



24th ABCM International Congress of Mechanical Engineering December 3-8, 2017, Curitiba, PR, Brazil

# COBEM-2017-0851 USING FOAM-EXTEND TO ASSESS THE INFLUENCE OF FLUID-SOLID INTERACTION ON THE FLOW IN INTRACRANIAL ANEURYSMS

## Iago Lessa de Oliveira José Luiz Gasche

São Paulo State University (UNESP) School of Engineering, Ilha Solteira, São Paulo, Brazil iago.42lessa@gmail.com gasche@dem.feis.unesp.br

#### Julio Militzer

Dalhousie University, Department of Mechanical Engineering, Halifax, Nova Scotia, Canada julio.militzer@dal.ca

#### Carlos Eduardo Baccin

Interventional Neuroradiology, Hospital Israelita Albert Einstein, São Paulo, Brazil cebaccin@gmail.com

Abstract. Aneurysms are abnormalities formed in some regions of the human vascular system and are characterized by dilated and thin regions of the arterial wall. One of the most common types occurs inside the brain arteries in the circle of Willis. These intracranial aneurysms are extremely dangerous because in case of rupture they can cause sub-arachnoid hemorrhage, with consequent death or presence of permanent damage to the patient. Causes of aneurysms have been investigated for a long time, and researchers agree that hemodynamic effects play a key role in the rupture of brain aneurysms. With the development of scanning techniques of the cerebral vascular system, it has been possible to obtain the geometry of aneurysms allowing numerical methods for the solution of blood flow to be used. Since then, several researchers have been investigating the influence of biological and hemodynamic variables on aneurysms rupture considering arteries and aneurysms as rigid walls. It has been only in the last decade that few works started investigating the influence of flexible walls – that is, including the fluid-structure interaction problem – on those variables. In this work we simulated the blood flow in patient-specific aneurysm geometries using the open-source library foam-extend-4.0 to numerically solve the fluid-structure interaction problem. By comparing the flow parameters – wall shear stress and flow impingement on the aneurysm wall – between the results of the simulations considering rigid and flexible walls hypotheses, we evaluated the influence of wall flexibility on such parameters, concluding that the flexibility of the walls influences the flow parameters that can lead to rupture.

Keywords: Intracranial aneurysms, numerical simulation, fluid-structure interaction, foam-extend

#### 1. INTRODUCTION

Aneurysms are arterial abnormalities defined as dilated regions of the artery wall. These abnormalities can arise at different sites of the human vascular system, more commonly found on the abdominal aorta and arteries that reach the brain. Intracranial aneurysms generally occur on arterial bifurcations located in the base of the brain, in the circle of Willis – formed by the internal carotid arteries, the vertebro-basilar system and their branches – or at nearby locations and their size can vary from 1 mm to 25 mm and even larger. Figure 1a shows a schematic figure of an aneurysm with its main geometric parameters and Fig. 1b depicts the brain vessels tree.

The rupture of intracranial aneurysms represent a high risk to the patient: they cause a mortality rate between 40 and 50% and also present high morbidity risk (permanent injury). It is also estimated that 2 to 3% of the world's population have intracranial aneurysms (Qureshi *et al.*, 2007). It is reported that 85% of Subarachnoid Hemorrhage (SAH) cases, a devastating event that can be fatal or lead to a severe neurological deficit, are caused by the rupture of these aneurysms (Gijn and Rinkel, 2001; van Gijn *et al.*, 2007; Zacharia *et al.*, 2010). Hop *et al.* (1997) concluded that fatal cases of SAH occurred from 32 to 67% and about one-third of morbidity among the patients who survived. The work of The International Study of Unruptured Intracranial Aneurysms Investigators (2003), one of the most relevant scientific works on rupture of intracranial aneurysms being used until today for the decision of their treatment, evaluated the probability of SAH over time for a group of 1,077 patients – followed up over 4.1 years – who had no previous cases of SAH, for

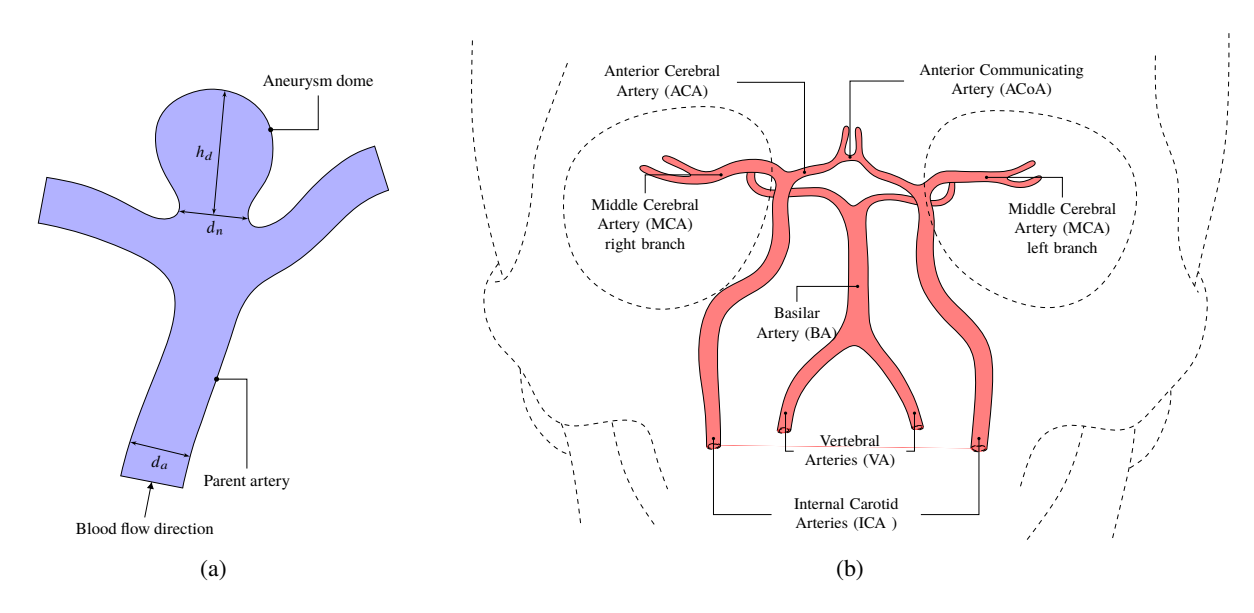


Figure 1. (a) Aneurysm dome, its parent artery and aspect ratio,  $A_r$ , definition: aneurysm dome height,  $h_d$ , divided by  $d_n$ , the neck diameter; the parent artery has diameter  $d_a$ ; (b) Frontal view of the skull with the location of the main arteries of the brain arteries tree, with the most common bifurcations where aneurysms can grow.

different aneurysm sizes and concluded that the risk of SAH increases over time and for larger aneurysms. The same study reported that, of the 193 patients who died during the follow up period, 27% died of intracranial hemorrhage.

Currently, the two major treatment techniques for intracranial aneurysms are surgical intervention – direct clipping, for example – and endovascular treatment – placement of coils inside the aneurysm dome and intra-vascular stent placement or occlusion of the parent vessel (Qureshi *et al.*, 2007). However, these interventions also present risks to patients. According to Torii *et al.* (2006), risks of permanent damage and death due to treatment and post-operative procedures are about 10%. Hence, one should evaluate the best alternative for the patient using a methodology that could provide more precise criteria for the recommended treatment. Currently, physicians use statistical methods based primarily on the size of the aneurysm – its dome height,  $h_d$  – to assess the probability of rupture.

Although the factors that lead to the rupture of intracranial aneurysms are still not well understood, more recent studies agree that the effects of blood flow inside the vessels (hemodynamic) are crucial for the development of these processes (Penn *et al.*, 2011; Meng *et al.*, 2014). The most relevant hemodynamic parameters taken into account in these studies are: the Wall Shear Stress (WSS) due to the flow velocity gradient adjacent to the aneurysm wall and its gradient, flow patterns inside the dome such as the jet impingement on the aneurysm wall, the Oscillatory Shear Index (OSI), hydrostatic pressure, transmural pressure – difference between the pressure inside and outside the artery wall – and flow vorticity. The problem is how to obtain these parameters.

With the development of computational imaging techniques – such as three-dimensional (3D) Digital Subtraction Angiography (DSA), 3D Rotational Angiography, Magnetic Resonance Angiography and Computed Tomography Angiography (Cebral and Cerrolaza, 2003; Wong and Poon, 2011) –, the geometry of patient-specific intracranial aneurysms can be obtained, allowing numerical simulations of the flow in realistic blood vessels and aneurysms through Computational Fluid Dynamics (CFD) (Steinman *et al.*, 2003; Shojima *et al.*, 2004; Castro *et al.*, 2006; Torii *et al.*, 2008; Bazilevs *et al.*, 2010; Lu *et al.*, 2011; Evju *et al.*, 2013; Karmonik *et al.*, 2014; Byrne *et al.*, 2014; Fukazawa *et al.*, 2015). Since the flow in aneurysms presents complex geometries, unsteady flow and complex rheological behavior, limited computational power prevented the use of CFD in the early simulations of flows in aneurysms for a large number of patients. However, with the fast increase in processing power of current computers, CFD is becoming suitable for studying particular cases of aneurysms.

In recent studies, researchers included the vessel wall motion in the numerical model (Bazilevs *et al.*, 2008, 2010; Lee *et al.*, 2013; Torii *et al.*, 2007, 2008, 2009; Tricerri *et al.*, 2015), accounting for the interaction between the blood flow and the artery and aneurysm wall flexibility, i.e. resolving the actual Fluid-Structure Interaction (FSI) problem. Bazilevs *et al.* (2010) compared the results of WSS obtained for rigid and flexible wall models and found that there is an overestimation of the WSS value of up to 36% if the vessel walls are considered rigid, indicating that to obtain more accurate values of the hemodynamic parameters, rigid wall may be a very crude assumption.

The objective of this work is to use CFD techniques to perform numerical simulations of two patient-specific aneurysms, resolving the actual FSI problem to evaluate its influence on physical parameters related to the flow in intracranial aneurysms and to its rupture – such as WSS and the flow patterns in the aneurysm – for different wall models: rigid and flexible wall.

#### 2. METHODOLOGY

#### 2.1 Problem Domain

We model the geometry of the aneurysm problem as a domain  $\Omega$ , with boundary  $\Gamma$ , composed of a solid domain  $\Omega^s$  – the artery wall – and a fluid domain  $\Omega^f$  – the blood flowing –, i.e.  $\Omega = \Omega^s \cup \Omega^f$ , with solid and flow boundaries indicated by  $\Gamma^s$  and  $\Gamma^f$ , respectively, as shown schematically in Fig. 2, which also shows the physical conditions applied to each boundary. The figure also shows the fluid-solid interface  $\Gamma^{fs} = \Gamma^f \cap \Gamma^s$ . The properties of the fluid are the density  $\rho^f$  and the dynamic viscosity  $\mu^f$  (with kinematic viscosity  $\nu^f$ ), while the properties of the solid material are represented by its density  $\rho^s$ , Young's modulus E and Poisson's ratio  $\nu^s$ .

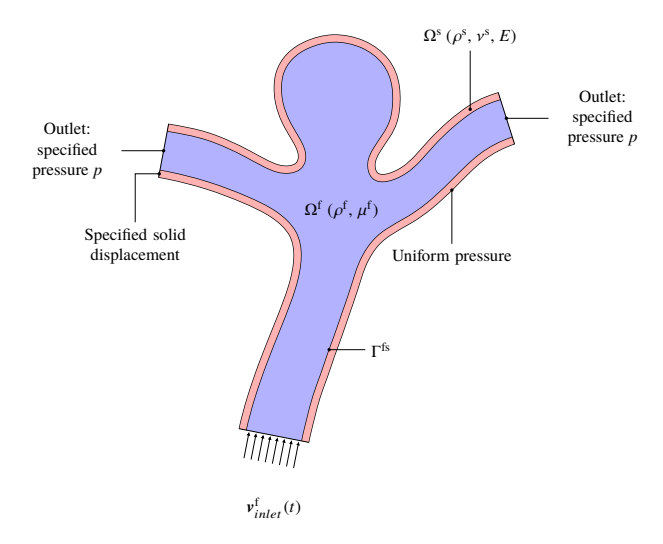


Figure 2. Solid,  $\Omega^s$ , and fluid domains,  $\Omega^f$ , fluid-solid interface  $\Gamma^{fs}$  and boundaries of each region with its respective physical boundary condition.

## 2.2 Physical and Mathematical Model of the Blood Flow

We consider the blood as an incompressible Newtonian fluid with constant dynamic viscosity, in an isothermal laminar flow regime – the velocities found in an aneurysm flow yield a Reynolds number, Re, of about 600 to 700 based on the parent artery diameter. The blood density and kinematic viscosity were considered to be 1,000 kg/m<sup>3</sup> and  $3.3 \times 10^{-6}$  m<sup>2</sup>/s, respectively (Isaksen *et al.*, 2008).

Since the flow domain can change in time due to the artery and aneurysm motion, the flow governing equations are presented in the Arbitrary Lagrangian-Eulerian (ALE) formulation (Belytschko *et al.*, 2014; Donea *et al.*, 1999), which uses the reference coordinate system,  $\chi$  to describe the movement of the domain. The equations governing the fluid motion are the continuity equation for incompressible flows, derived from mass conservation principle, written in integral form for a moving control volume V = V(t), with surface S, as:

$$\oint_{S(t)} \rho^{f} \mathbf{v}^{f} \cdot \mathbf{n} dS = 0 \tag{1}$$

where n is the unit normal vector to S pointing outwards and  $v^f$  is the flow velocity field. For a moving frame of reference, mass conservation is written as in Eq. (1) if the moving control volume V(t) satisfies the *geometric conservation law* (Demirdžić and Perić, 1988):

$$\frac{\partial}{\partial t}\Big|_{X} \int_{V(t)} dV = \oint_{S(t)} \omega \cdot \mathbf{n} dS \tag{2}$$

where  $\omega$  is the velocity of the surface of the control volume; the momentum equation, derived from the balance of linear momentum in integral conservative ALE form for a Newtonian fluid with constant properties is written as:

$$\frac{\partial}{\partial t} \Big|_{X} \int_{V(t)} \rho^{f} v^{f}(x, t) dV + \oint_{S(t)} \rho^{f} v^{f} \left(v^{f} - \omega\right) \cdot n dS = -\oint_{S(t)} p n dS + \oint_{S(t)} \mu^{f} \nabla v^{f} \cdot n dS$$
(3)

where the bar with  $\chi$  on the temporal term means that the derivative is calculated with  $\chi$  fixed and p is the pressure.

# **Boundary and Initial Conditions**

A trivial initial condition is usually used, however we chose to use the numerical solution of the flow velocity and pressure fields from a numerical simulation considering the aneurysm wall as rigid. The conditions at each domain boundary are shown in Fig. 2. For velocity and pressure in the flow domain, they are:

• Inlet: the inlet is a cross section located in the parent artery of the aneurysm (Fig. 2) which depends on the aneurysm branch location. The condition imposed is a specified time-varying velocity, corresponding to the flow pulse from the beginning of systole until the end of the diastole. Such waveform profile, measured in the internal carotid by Ford *et al.* (2005), is shown in Fig. 3a as a normalized flow rate based on the temporal average blood flow rate. Since the aneurysms studied here are located in different bifurcations of the brain vessels tree, we calculated the inlet velocity multiplying this normalized flow rate by the average blood flow rate of the artery of interest. The average blood flow rate,  $\bar{q}_a$ , for different portions of the brain vessels tree was provided by Zarrinkoob *et al.* (2015), who measured it as a percentage of the total blood flow rate to the brain vessels for normal subjects (11.95  $\pm$  2.05) ml/s, as shown in Fig. 3b, which presents the mean and the standard deviation values. Finally, the velocity profile was computed using the known cross sectional area of the inlet section (calculated from the fluid mesh). At the inlet, the pressure gradient was set to zero.

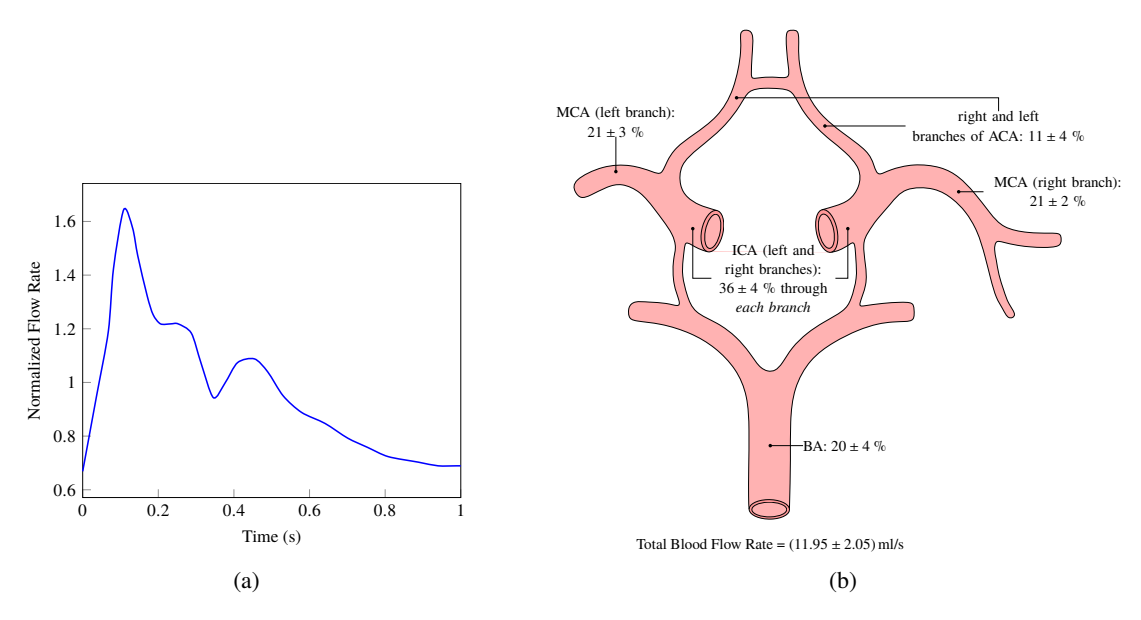


Figure 3. (a) Experimental normalized flow rate for the internal carotid (prepared by the authors with data provided by Ford *et al.* (2005)); (b) Average blood flow rate through the arteries of the brain as a percentage of the total blood flow rate entering the brain, with each respective standard deviation (prepared by the authors with data from Zarrinkoob *et al.* (2015)).

- Outlets: the outlets are located on the vessels after the aneurysm bifurcation. Even for incompressible flow, it is important to use the actual level of pressure in the FSI context because this information is interpolated as a boundary condition for the solid problem. Therefore, we specified a constant pressure, equal to the average pressure level in the human body ≈ 100 mmHg (13,333 Pa);
- Wall: This boundary corresponds to the FSI interface,  $\Gamma^{fs}$ . We present this boundary condition in details in Section 2.4.

#### 2.3 Physical and Mathematical Model of the Artery and Aneurysm Wall Tissue

The solid domain of the problem is the artery and aneurysm walls with a specified uniform thickness found in the literature and we chose the elastic linear isotropic model to describe its mechanical behavior.

The mechanical properties of the wall tissue were considered uniform and constants:  $\rho^s = 1,000 \, \text{kg/m}^3$ ,  $E = 1 \, \text{MPa}$  and  $v^s = 0.45$  (Isaksen *et al.*, 2008). A uniform thickness of 0.15 mm for the aneurysm and artery wall was used. We relied on values found in the literature because the measurement of these properties, like Young's modulus and Poisson's ratio for example, of living tissues is still difficult. Moreover, the wall thickness is also hard to measure due to poor resolution of the images used.

The governing equation for each model is derived from the balance of linear momentum and it is written in the following form for a deformable solid under defined boundary conditions in *total Lagrangian* formulation (Belytschko *et al.*, 2014) with displacement field u:

$$\rho_0^s \frac{\partial^2 \boldsymbol{u}}{\partial t^2} = \rho_0^s \boldsymbol{g} + \nabla_0 \cdot \boldsymbol{P} \tag{4}$$

where g is the gravitational acceleration (accounting as a body force) and P is the *nominal stress tensor*, a multiaxial extension of the engineering stress and  $\rho_0^s$  is the *initial* solid density. We use the lower script "0" for differential operators calculated at the initial material configuration, which is represented by the material coordinates  $\xi$  (Belytschko *et al.*, 2014).

To close the solid problem formulation, we invoke a constitutive equation for the solid. We used the isotropic elastic model with linear (small deformations) behavior, and its constitutive equation is given by Hooke's law:

$$\sigma^{s} = 2\mu^{s} \varepsilon + \lambda^{s} tr(\varepsilon) \mathbf{I}$$
 (5)

where  $\mu^s$  and  $\lambda^s$  are the Lamé's constants; I is the second order identity tensor;  $\sigma^s$  is the Cauchy stress tensor – or true stress –, which is related to the multiaxial nominal stress by the following equation:

$$\sigma^{s} = \frac{1}{\det(\mathbf{F})} \mathbf{F} \cdot \mathbf{P} \tag{6}$$

where F is the deformation gradient tensor (Belytschko *et al.*, 2014). The linear strain tensor,  $\varepsilon$ , is a function of the solid displacement u:

$$\boldsymbol{\varepsilon} = \frac{1}{2} \left( \nabla_0 \boldsymbol{u} + \nabla_0^T \boldsymbol{u} \right) \tag{7}$$

Combining Eq. (4) with the constitutive equation and strain tensor definition yields a partial differential equation for the solid displacement u, which is the equation solved for the solid part of the FSI aneurysm problem.

# **Boundary and Initial Conditions**

The initial condition, as for the fluid case, is the numerical solution of the simulation considering only the wall as part of the problem. Using the stress distribution on the wall from the flow solution, a displacement field is obtained and hence used as initial condition. The following boundary conditions were used:

- For the adjacent sections of the arteries see Fig. 2 –, the displacement was set to zero;
- Internal and external surfaces of the aneurysm and artery walls: a Neumann boundary condition was used, derived from the elastic linear constitutive relation:

$$\boldsymbol{t}^{\mathrm{s}} = \left[ (2\mu^{\mathrm{s}} + \lambda^{\mathrm{s}}) \nabla_{0} \boldsymbol{u} + \mu^{\mathrm{s}} \nabla_{0}^{T} \boldsymbol{u} + \lambda^{\mathrm{s}} tr(\nabla_{0} \boldsymbol{u}) \boldsymbol{I} - (\lambda^{\mathrm{s}} + \mu^{\mathrm{s}}) \nabla_{0} \boldsymbol{u} \right] \cdot \boldsymbol{n}^{\mathrm{s}}$$
(8)

where  $t^s$  is the traction on the surface, which depends on the stresses and pressure acting on the surface and  $n^s$  is the unit normal vector to the surface pointing outwards. Rearranging Eq. (8) yields:

$$(\nabla_0 \boldsymbol{u}) \cdot \boldsymbol{n}^s = \frac{\boldsymbol{t}^s - \left[ \mu^s \nabla_0^T \boldsymbol{u} + \lambda^s tr(\nabla_0 \boldsymbol{u}) \boldsymbol{I} - (\lambda^s + \mu^s) \nabla_0 \boldsymbol{u} \right] \cdot \boldsymbol{n}^s}{2\mu^s + \lambda^s}$$
(9)

that corresponds to a displacement gradient specification. The gradients in the right hand side of Eq. (9) are calculated explicitly.

On the inner surface of the aneurysm and artery walls – the FSI interface –,  $t^s$  is evaluated using the dynamic condition at the FSI interface, as will be show in Section 2.4.

On the outer surface, Eq. (9) still applies, however the traction  $t^s$  is due only to an uniform pressure applied on it, according to:

$$t^{s} = -pn^{s} \tag{10}$$

where p on the outer surface is approximately 5 mmHg and corresponds to the intracranial pressure.

# 2.4 Physical Condition on the FSI interface

Regarding the boundary condition on the fluid-solid interface, the formulation presented is usually called *Dirichlet-Neumann formulation* of the FSI problem because the flow equations are solved for a specified velocity at  $\Gamma^{fs}$  due to the kinematic condition that guarantees the continuity of velocity at this boundary:

$$(v^{f})_{\Gamma^{fs}} = (v^{s})_{\Gamma^{fs}} = \left(\frac{\mathrm{d}u}{\mathrm{d}t}\right)_{\Gamma^{fs}}$$
 (11)

whereas the solid equation is solved with an imposed traction on  $\Gamma^{fs}$  due to the dynamic condition of traction continuity at the interface, expressed as:

$$\underbrace{\left(\boldsymbol{\sigma}^{\mathrm{f}} \cdot \boldsymbol{n}^{\mathrm{f}}\right)_{\Gamma^{\mathrm{fs}}}}_{\boldsymbol{t}^{\mathrm{f}}} + \underbrace{\left(\boldsymbol{\sigma}^{\mathrm{s}} \cdot \boldsymbol{n}^{\mathrm{s}}\right)_{\Gamma^{\mathrm{fs}}}}_{\boldsymbol{t}^{\mathrm{s}}} = \boldsymbol{0}$$
(12)

and therefore, this last condition gives  $t^s$  of Eq. (9). In Eq. (12),  $n^f$  and  $n^s$  are the normal vectors on  $\Gamma^{fs}$  pointing outwards, respectively, of the solid and fluid domain.

#### 2.5 Domain Discretization

The patient-specific aneurysms geometries were extracted from digital subtraction angiographic (DSA) studies, using the open-source package  $VMTK^{\circledast}$ , which also generated the computational meshes used. Figure 4 shows the sequence of steps performed in  $VMTK^{\circledast}$  for generating the final surface, which was used to create the fluid and solid meshes, for one of the cases studied here: first, the whole surface of the vessels tree is extracted as a surface computational, which is then segmented for obtaining only the region where the aneurysm is located and, finally, extracting the final aneurysm and surrounding vessels surface. The fluid mesh is then created using Netgen (an open-source automatic tetrahedral mesh generator) and the solid mesh is created by extrusion of the surface using the utility extrudeMesh of foam-extend-4.0, the package used for the FSI simulations.

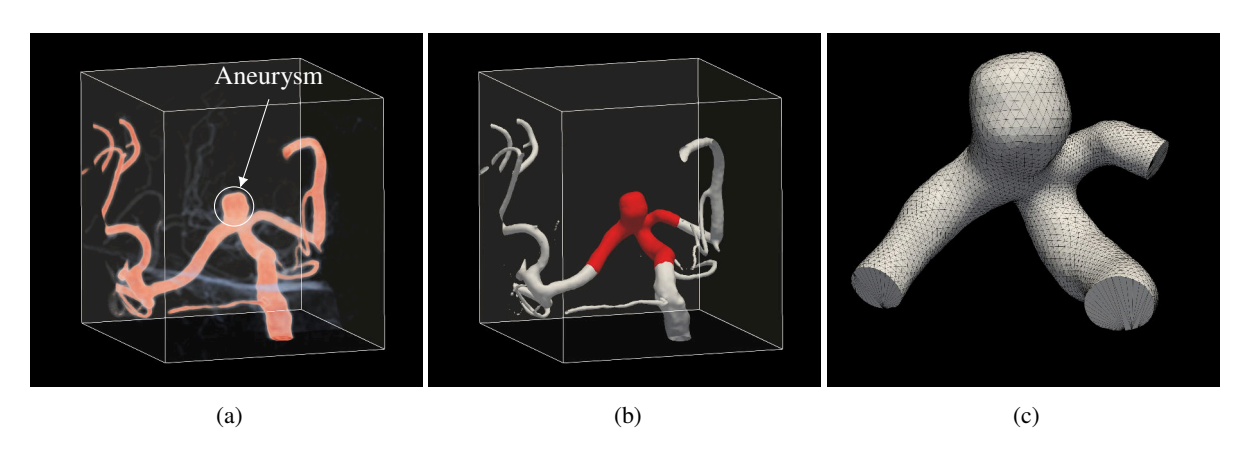


Figure 4. (a) Volume rendering representation of the DSA image of the aneurysm and surrounding vessels (rendered in ParaView®); (b) Segmented surface using VMTK® (as a red surface); (c) final extracted portion of the surface containing the aneurysm geometry.

The geometries of the aneurysms studied here, which we name as "case 13" and "case 11", are shown in Fig. 5. Table 1 provides the geometric characteristics of these aneurysms such as height  $h_d$ , neck diameter  $d_n$ , parent artery, aspect ratio defined as the dome height divided by the neck diameter, and mean blood flow rate in the parent artery. The table also shows the total number of cells of the fluid and solid meshes of each case.

## **Fluid Mesh Motion**

The fluid mesh must be updated according to the movement of the solid (artery and aneurysm), therefore is recommended to use a dynamic mesh methodology to avoid large distortions of the cells. We used a method based on the Laplace equation's solution for the velocity of cell centroids. This technique consists of solving the following equation:

$$\nabla \cdot (\gamma \nabla \omega) = 0 \tag{13}$$

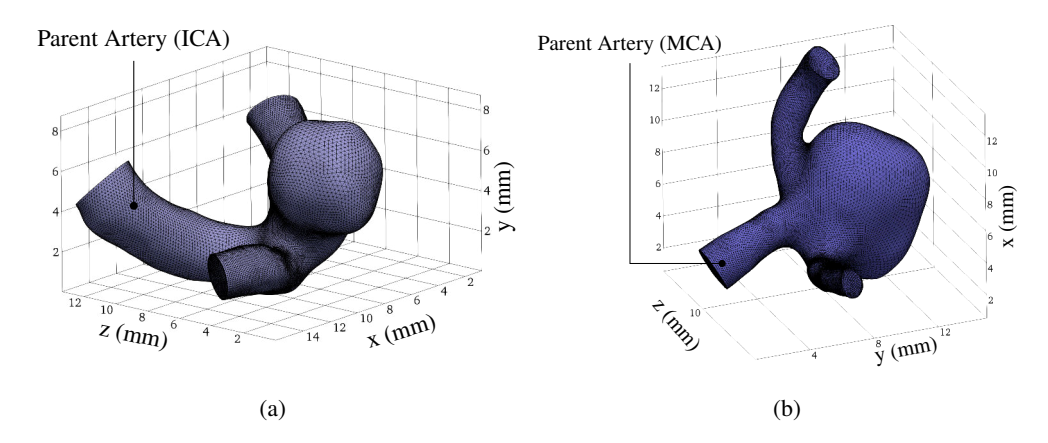


Figure 5. Aneurysm geometries used: (a) case 13, an aneurysm occurring on the ICA bifurcation and (b) case 11, occurring on the bifurcation of the MCA.

Table 1. Geometric parameters of the aneurysms studied here: parent artery and its diameter  $d_a$ , neck diameter  $d_n$ , dome height  $h_d$  and diameter  $d_d$ , aspect ratio  $A_r$ , the mean blood flow rate through its parent artery,  $\bar{q}_a$  and the total number of cells in each mesh.

	Parent Artery	$d_n$ (mm)	$h_d$ (mm)	$d_d$ (mm)	da (mm)	$A_r$ (-)	$\bar{q}_a$ (ml/s)	Number of Elements	
								Fluid Mesh	Solid Mesh
case 13	Right ICA	4.3	5.7	5.0	3.1	1.3	4.3	628,565	117,744
case 11	MCA	7.0	7.9	7.1	2.8	1.3	2.5	786,002	133,248

where  $\gamma$  is a "mesh diffusivity";  $\omega$  is the control volume centroid velocity. We used a distance-based approach where  $\gamma$  is given by:

$$\gamma = \frac{1}{l^2} \tag{14}$$

where l is the cell centroid distance to a selected moving boundary which is, for the aneurysms simulations, the aneurysm wall – the fluid-solid interface. As presented by Jasak and Tuković (2006) this approach leads to a more "rigid" mesh close to the selected boundary because  $\gamma$  is higher, preserving the original quality of the cells. Since we used a refined layer of prismatic elements close to the aneurysm and vessels walls, this is the desired behavior.

The boundary conditions for  $\omega$  are: on inlets and outlets we specify zero velocity conditions. For the aneurysm wall, which is the fluid-solid interface, the velocity boundary condition is interpolated from the solid displacement of the last coupling iteration.

After solving Eq. (13), the cell centroid velocity,  $\omega$ , is interpolated from the cell centroid to the geometric nodes. We call this interpolated velocity  $\omega_{node}$ . Finally, the mesh nodes coordinates are updated by:

$$x_{new} = x_{old} + \omega_{node} \Delta t \tag{15}$$

where  $\Delta t$  is the time-step of the flow numerical simulation,  $x_{new}$  and  $x_{old}$  are the mesh nodes position after and before solving the equation, respectively.

# 2.6 Numerical Methods and Data Analysis

To solve the system of equations governing the FSI problem – Eqs. (1), (3) and (13) with the solid equation – under the boundary conditions presented in Sections 2.2, 2.3, and 2.4we chose the Finite Volume Method (FVM) (Patankar, 1980; Moukalled *et al.*, 2016), since it is one of the most used numerical methods for CFD applications and is starting to be used for Solid Mechanics problems (Cardiff, 2012; Cardiff *et al.*, 2016). We used the open-source package foam-extend (OpenFOAM-Extend, 2017), version 4.0, which has a specific extension providing a solver for FSI problems.

The foam-extend package uses the FVM with collocated variables arranged in a cell-centered discretization of the governing equations. A finite-volume mesh is composed of non-overlapping polyhedral cells with polygonal flat faces and each internal face is shared by two cells; external faces, which compose the boundaries of the domain, belong to only one cell. The meshes presented in Section 2.5 follow these conditions. The complete discretization process of the FVM can be found in more specific literature such as Moukalled *et al.* (2016) and Versteeg and Malalasekera (2007).

To couple the governing equations through the FSI interface, we used a partitioned methodology implemented in foam-extend, which consists of solving the flow problem, Eqs. (1) and (3), the solid problem, and the mesh motion equation, Eq. (13), separately and sequentially with the conditions at the fluid-solid interface, Eqs. (11) and (12), obtained interpolating each solution at this interface. One of the main advantages of this approach is the ability to re-use algorithms already developed, allowing different discretization for each domain if needed. Therefore, two computational meshes are provided and the rest of the work consists of building an algorithm that performs interpolation of variables between the FSI interface of each mesh. Figure 6 shows an example of a computational mesh of an aneurysm domain  $\Omega$  for a FSI problem treated in a partitioned manner: the fluid and solid meshes are separated and have the FSI interface,  $\Gamma^{fs}$ , in common; we call  $\Gamma^{fs}_{fluid}$  the fluid mesh boundary that corresponds to the FSI interface and  $\Gamma^{fs}_{solid}$  for the solid mesh. The same figure also shows the interpolation of variables between these surfaces: after solving the governing equations of the flow, the pressure p and traction t fields are interpolated from  $\Gamma^{fs}_{solid}$  to  $\Gamma^{fs}_{solid}$ ; on the other hand, once the solution of the governing equation of the solid is known, the displacement u and velocity v at  $\Gamma^{fs}_{solid}$  are interpolated to  $\Gamma^{fs}_{fluid}$ .

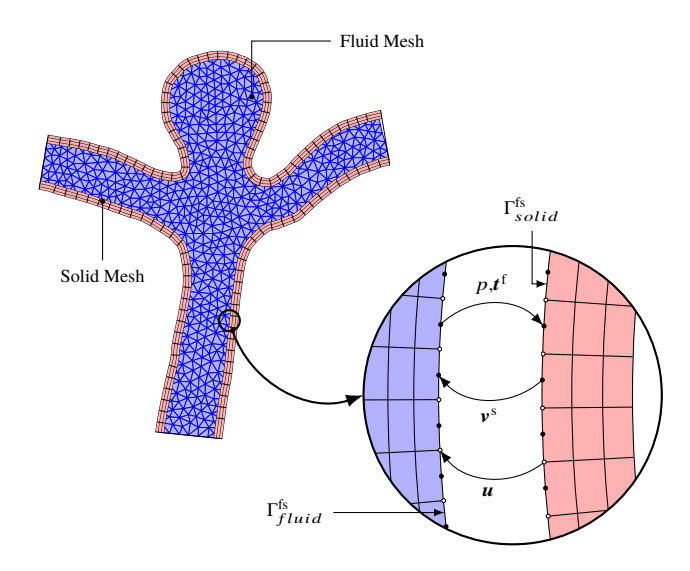


Figure 6. Schematic two-dimensional representation of the fluid and solid meshes of an aneurysm geometry showing each FSI interface and the interpolated variable between the solid and fluid mesh interfaces.

Although flexible, partitioned methodologies are very unstable (Bazilevs *et al.*, 2012), especially for problems with strong physical couplings between the fluid and structure, e.g., high fluid and solid density ratio, which occurs when the solid is very light compared to the fluid, and/or incompressible flow leads to unconditionally instability of the computational solution (Degroote *et al.*, 2008; Causin *et al.*, 2005). This is exactly the case with the aneurysm flow problem. In general, coupling schemes are applied in these situations to improve solution stability.

We chose to use a robust procedure, proposed by Degroote *et al.* (2009) and implemented in foam-extend, called Interface Quasi-Newton-Implicit Jacobian Least-Squares (IQN-ILS) to couple the equations. This procedure solves a residual form of the equation that governs the position of the FSI interface in each time-step, using quasi-Newton iterations and approximating the product of the *inverse* of the Jacobian by the residual vector through a least-squares method. The complete procedure is presented by Degroote *et al.* (2010).

Once completed the simulations, we visualized the flow velocity and WSS fields, the last one calculated as  $WSS = \|WSS\|_2 = (\|\tau \cdot n^f\|)_{\Gamma^{fs}}$ , using ParaView<sup>®</sup>, an open-source software for post-processing of CFD simulations. This software has a large number of filters that allow processing and displaying all field variables of the flow, of the solid, and of the wall-fluid interface.

#### 3. RESULTS

#### 3.1 Mesh-independence analysis

Regarding code verification analysis (Oberkampf and Trucano, 2002), foam-extend is widely used in industrial and academic research and has been tested in several fields. For FSI problems solved using an extension of the code, three benchmark cases were provided with the latest release. Regarding validation of the numerical solution, unfortunately, we were not able to validate the results experimentally. The other requirement is the verification of the numerical accuracy of the simulations presented here. In the rest of this section, we analyze the numerical accuracy of our results through a mesh-independence analysis.

We evaluated mesh-independence of the numerical solution qualitatively, comparing the spatial distribution of WSS

on the aneurysm surface, and quantitatively using the surface area averaged WSS over the surface of the geometries used. To perform this study, we solved the flow considering the rigid wall assumption. The meshes of all cases were tested, but for brevity we illustrate the procedure here only for cases 13.

Figure 7 shows the WSS on the surfaces for meshes with  $\sim 300,000$ ,  $\sim 600,000$ , and  $\sim 1,000,000$  control volumes for case 13. We see in the figure that there are small qualitative differences regarding the WSS for meshes with  $\sim 600,000$  and  $\sim 1,000,000$  control volumes, i.e. the overall pattern of the WSS field is already established for the mesh with  $\sim 600,000$  control volumes, suggesting that this level of refinement is adequate. Figure 8, on the other hand, shows how the area-averaged WSS over the whole mesh surface varies with time, for two cardiac cycles, where the area averaged WSS is given by:

$$\overline{WSS}_S = \frac{1}{A_S} \left\| \int_S (WSS) \, \mathrm{d}S \right\|_2 \tag{16}$$

where S is the wall surface and  $A_S$  its area. Results show that there are only small differences of the area-averaged WSS for the three meshes. Therefore, we conclude that the fluid mesh with  $\sim 600,000$  is sufficiently refined to provide accurate results, at least for the WSS field, which is the main parameter studied here.

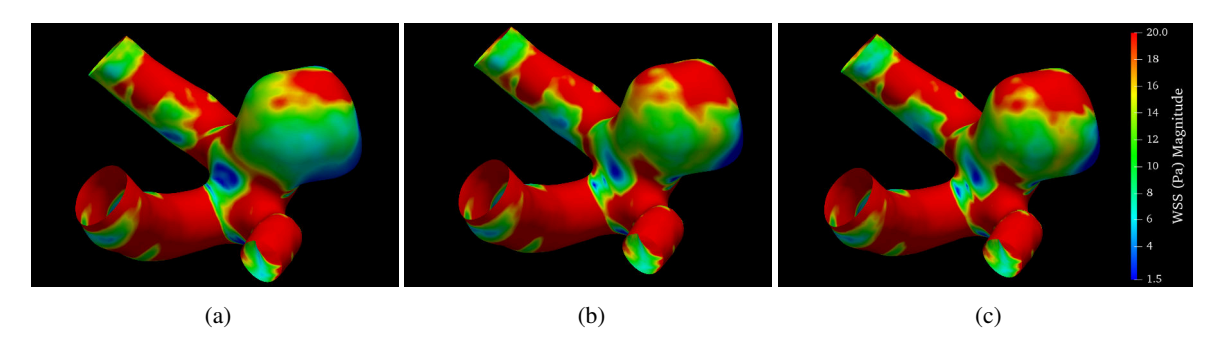


Figure 7. WSS magnitude distribution on the surface of the aneurysm of case 13 for fluid meshes with (a)  $\sim 300,000$ , (b)  $\sim 600,000$  and (c)  $\sim 1,000,000$ .

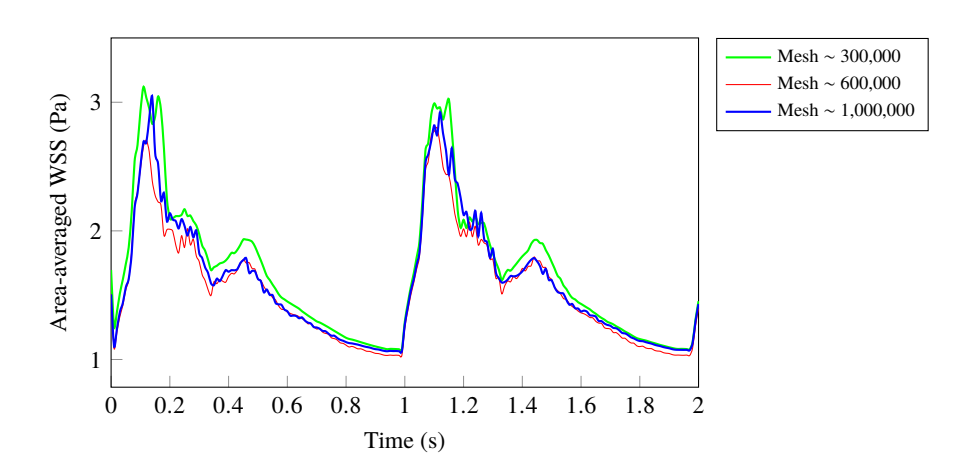


Figure 8. Area-averaged WSS as a function of time for the whole surface for case 13 fluid mesh, with total number of control volumes  $\sim 300,000$ ,  $\sim 600,000$  and  $\sim 1,000,000$  to test mesh independence of the averaged WSS.

Although it would be more appropriate to still use meshes with a higher degree of refinement – number of control volumes greater than 1,000,000 – however, we had to take into account a balance between adequate accuracy and reliability with reasonable computing time and resources requirements. For very fine meshes the required number of processing units increases considerably. Furthermore, the explicitness of the Interface Quasi-Newton-Implicit Jacobian Least-Squares (IQN-ILS) method for the FSI coupling requires the use of small time-steps to maintain stability of the technique. The range of time-step was chosen by observing the behavior of the evolution in time of the numerical solution, which seems to be stable if the maximum *Courant number*, *Co*, is smaller than 1. The Courant number is defined as the ratio:

$$Co = \frac{\|(\mathbf{v}^{\mathrm{f}})_f\|\Delta t}{\delta} \tag{17}$$

where  $\delta$  is a length defined for a cell; since foam-extend has support for generic polyhedral cells,  $\delta$  is defined as the projection of the vector joining adjacent cells centroids on the face normal direction. The condition Co < 1 is a well know condition for the stability of explicit temporal discretization techniques for advection problems. Although we used an implicit temporal discretization of the governing equations for the fluid and solid problems, the coupling iterations diverged when Co > 1. We did not find any reference in the literature for this connection between the Co and the stability of coupling FSI techniques, however the literature reports that the temporal discretization approach for the solid and fluid equations has influence in the stability of partitioned techniques (Förster *et al.*, 2006a,b), which could indicate a relation with the Courant number. Therefore, using Eq. (17) yields a time-step of  $1 \times 10^{-5}$  s for case 11 and  $0.5 \times 10^{-4}$  s for case 13.

# 3.2 Simulations Results

Figures 9 and 10 show the WSS and velocity fields for case 13, respectively. The scale was set up using a reference value of  $WSS \approx 1.5$  Pa, below which the WSS can degenerate endothelial cells and possibly lead to rupture, as concluded by Shojima *et al.* (2004). In Fig. 9a (rigid walls model) we identify a large region of low WSS on the back of the aneurysm dome, caused by a large recirculation zone due to the direction of the flow jet that enters the aneurysm: the jet collides with the neck – point A in Fig. 10a – causing a recirculating flow within the dome and, more precisely, in the region indicated by point B in Fig. 10a, which is the cause of the lower levels of WSS. However, in the flexible wall simulation, the low level of WSS in that region disappears – region A in Fig. 9b. In Fig. 10b, we see that the flow jet entering the aneurysm dome is less intense because part of its initial kinetic energy is lost due to the wall deformation, which changes the flow pattern inside the aneurysm dome, increasing the flow velocity – region B in Fig. 10b – hence increasing the WSS level on the aneurysm wall.

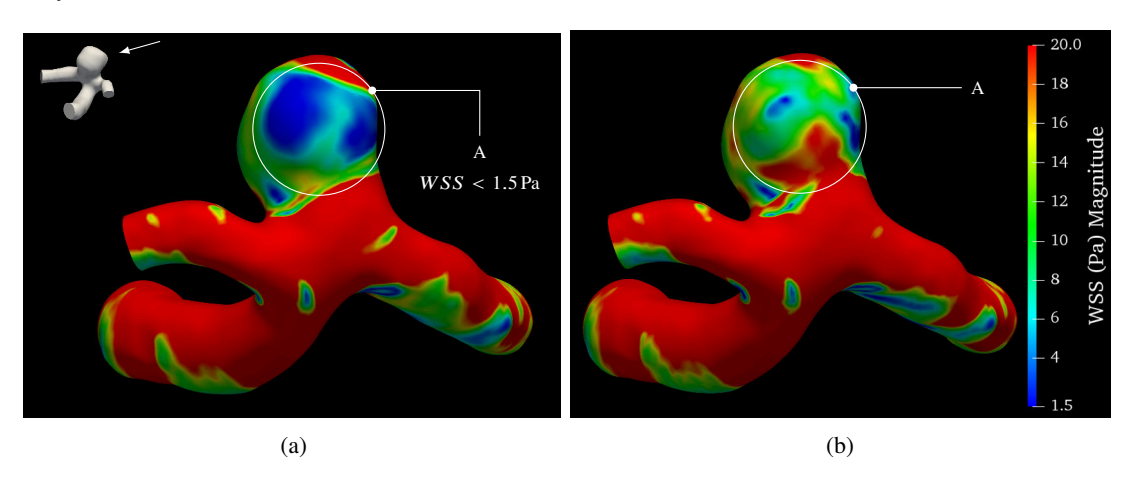


Figure 9. Comparison of WSS on the surface of case 13 with (a) rigid wall and (b) linear elastic wall models at peak systole (the white arrow at the top left corner indicates the direction of the view).

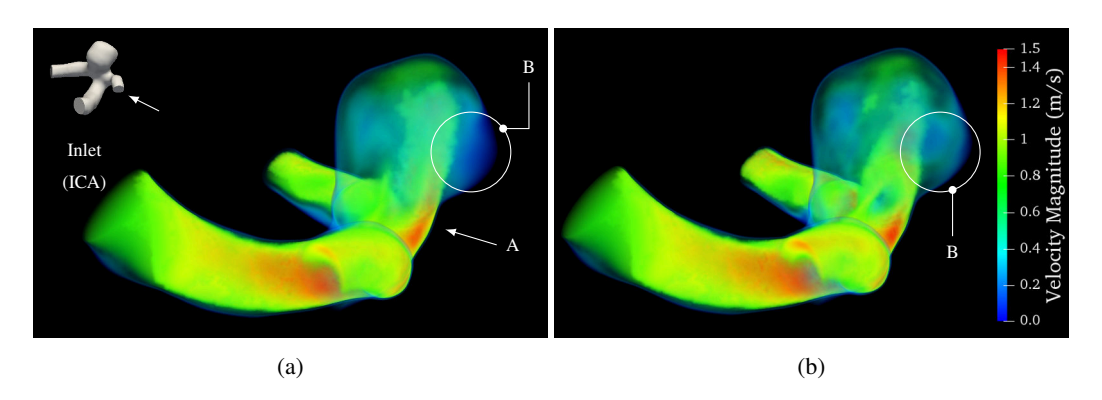


Figure 10. Volume rendering representation of the velocity field of the aneurysm of case 13 for (a) rigid wall assumption and (b) elastic linear wall model at peak systole; arrow A indicates the region of flow impingement, for this case occurring at the aneurysm neck.

Figure 11 shows the WSS for case 11 with rigid and linear elastic wall models. Also for this case, we observe that the WSS levels increase on the overall surface of the aneurysm when we use the linear elastic wall model. The velocity field

inside the dome of this aneurysms is more intense, because the flow jet impinges the aneurysm wall. More important is the fact that the WSS is remarkably higher than 1.5 Pa for the two cases when the flexible wall model is applied, which, as explained before, is a limit below which the vessels wall could be damaged.

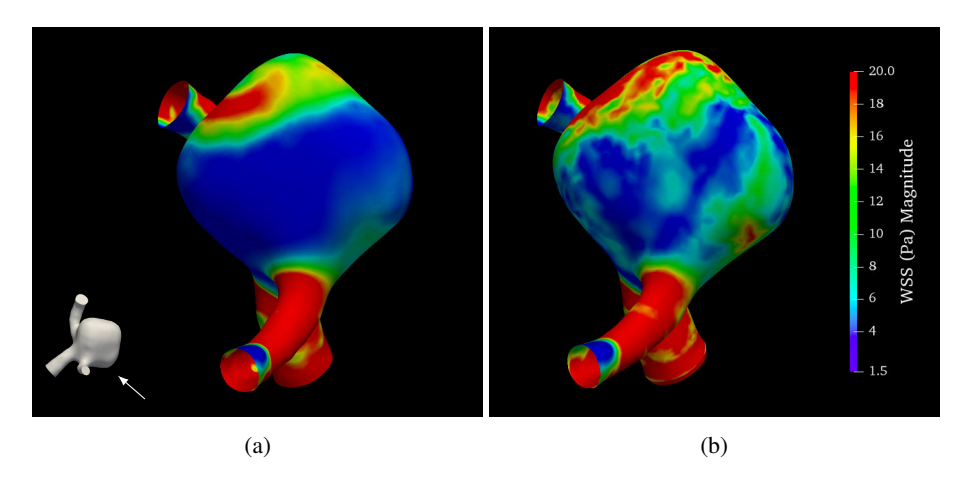


Figure 11. Comparison of WSS on the surface of case 11 (a) with rigid wall and (b) with linear elastic wall models at peak systole (the white arrow at the top left corner indicates the direction of the view).

Figure 12a shows a volume rendering representation of the velocity field of the flow for case 11 obtained with the rigid wall model at the peak systole ( $t = 0.1 \, \text{s}$ ), while Figs. 12b to 12d show the flow field of the same case obtained with the linear elastic solid model at the instants  $0.05 \, \text{s}$ ,  $0.1 \, \text{s}$  (peak systole), and  $0.15 \, \text{s}$ , respectively. Comparing Figs. 12a and 12c (at the same instant) it is possible to see that the level of velocity is higher for the FSI case, as shown for case 13, explaining the higher levels of WSS encountered (see Fig. 11b).

Another important feature of case 11, which has not occurred in the other case, is the jet flow impingement direction. The direction of the flow entering the aneurysm was investigated in numerical studies and some aspects of the flow patterns were related to rupture, such as flow impingement on the aneurysm dome (Cebral *et al.*, 2005). From the volume rendering representation, we can see that the flow enters the aneurysm dome and collides with the aneurysm wall (the jet in red in Figs. 12c and 12d). The important feature of this case is that the jet impinging the aneurysm completely changes its geometry due to the force caused by the jet, which rotates the dome to the right – the relative displacement is of the order of its parent artery diameter –, as we can see in Fig. 13a. In Figs. 12b to 12d, the gray surface indicates the original position of the aneurysm geometry. Finally, Fig. 13b shows the relative position of the aneurysm geometry at the initial instant and at instant 0.15 s of the cardiac cycle.

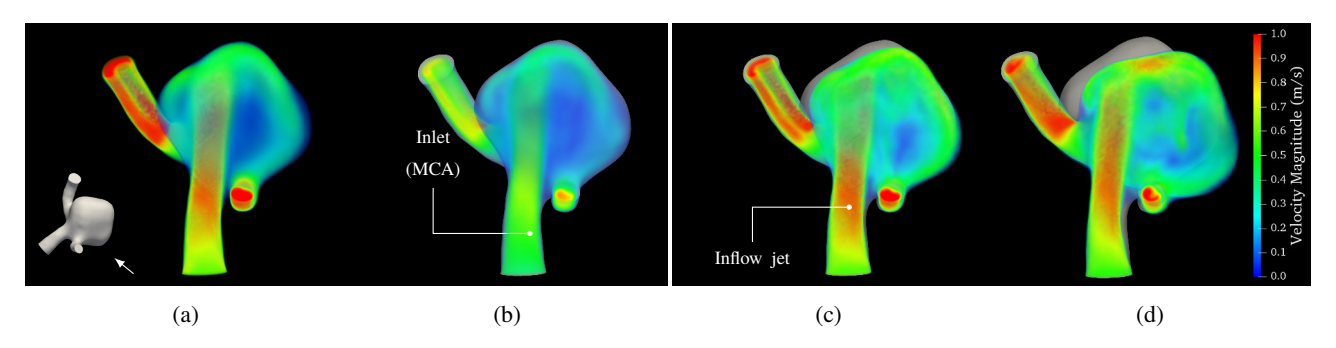


Figure 12. Volume rendering representation of the velocity field of case 11 (a) for the rigid wall model at peak systole and for the linear elastic model at the instants (b) 0.05 s, (c) 0.1 s (peak systole) and (d) 0.15 s of the cardiac cycle, showing the jet impingement at the aneurysm wall and the consequent geometry change of the aneurysm.

## 4. CONCLUSIONS

The results show that the flexible aneurysm wall model changes the values obtained for the hemodynamic parameters that may lead to aneurysm rupture. This can be explained once we know that the aneurysm fluid-solid problem is strongly coupled: the motion of the artery changes the fluid domain sufficiently to alter the flow variables in a significant way and, most importantly, the hemodynamic parameters usually related to aneurysms rupture. Therefore, we suggest that the flexible wall model should be used to simulate the flow in cerebral aneurysms because this can change the medical

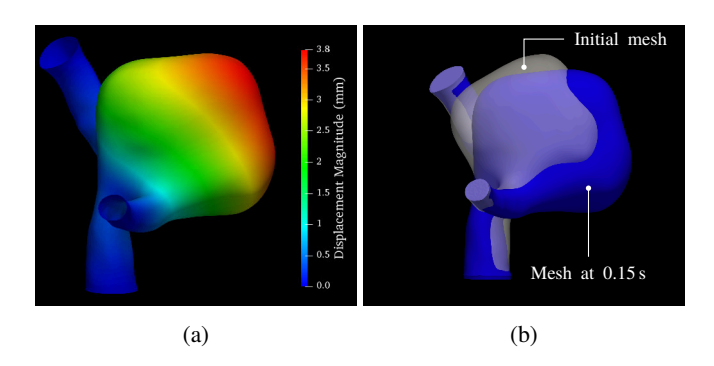


Figure 13. (a) Displacement field magnitude of aneurysm case 11 at instant 0.15 s of the cardiac cycle and (b) relative position of the aneurysm geometry for instants 0 s and 0.15 s of the cardiac cycle.

decision about the correct treatment of a patient: using the rigid wall model, the WSS levels are lower than the reference value and this would suggest some type of medical treatment; instead, if the flexible wall model is used, the WSS levels are higher and this would not suggest any type of medical treatment.

#### 5. ACKNOWLEDGEMENTS

This research was partly supported by resources supplied by the Center for Scientific Computing (NCC/GridUNESP) of the São Paulo State University (UNESP) and Acenet (Dalhousie University). This work was conducted with a scholarship financed by CAPES – Brazilian Federal Agency for Support and Evaluation of Graduate Education within the Ministry of Education of Brazil. Part of this work was developed at Dalhousie University, Nova Scotia, Canada, with support of the Government of Canada.

#### 6. REFERENCES

Bazilevs, Y., Calo, V.M., Hughes, T.J.R. and Zhang, Y., 2008. "Isogeometric fluid-structure interaction: Theory, algorithms, and computations". *Computational Mechanics*, Vol. 43, No. 1, pp. 3–37. ISSN 01787675. doi:10.1007/s00466-008-0315-x.

Bazilevs, Y., Hsu, M.C., Zhang, Y., Wang, W., Kvamsdal, T., Hentschel, S. and Isaksen, J.G., 2010. "Computational vascular fluid-structure interaction: Methodology and application to cerebral aneurysms". *Biomechanics and Modeling in Mechanobiology*, Vol. 9, No. 4, pp. 481–498. ISSN 16177959. doi:10.1007/s10237-010-0189-7.

Bazilevs, Y., Takizawa, K. and Tezduyar, T.E., 2012. *Computational Fluid-Structure Interaction: Methods and Applications*. John Wiley & Sons. ISBN 9780470978771. doi:10.1002/9781118483565.

Belytschko, T., Liu, W.K. and Moran, B., 2014. *Nonlinear Finite Elements for Continua and Structures*. John Wiley & Sons, 2nd edition. ISBN 0122030532. doi:10.1016/S0065-230X(09)04001-9.

Byrne, G., Mut, F. and Cebral, J., 2014. "Quantifying the large-scale hemodynamics of intracranial aneurysms". *American Journal of Neuroradiology*, Vol. 35, No. 2, pp. 333–338. ISSN 01956108. doi:10.3174/ajnr.A3678.

Cardiff, P., Tuković, Ž., Jasak, H. and Ivanković, A., 2016. "A block-coupled Finite Volume methodology for linear elasticity and unstructured meshes". *Computers and Structures*, Vol. 175, pp. 100–122. ISSN 00457949. doi: 10.1016/j.compstruc.2016.07.004.

Cardiff, P., 2012. *Development of the Finite Volume Method for Hip Joint Stress Analysis by Philip Cardiff.* Ph.D. thesis, University College Dublin.

Castro, M.A., Putman, C.M. and Cebral, J.R., 2006. "Computational fluid dynamics modeling of intracranial aneurysms: Effects of parent artery segmentation on intra-aneurysmal hemodynamics". *American Journal of Neuroradiology*, Vol. 27, No. 8, pp. 1703–1709. ISSN 01956108. doi:27/8/1703 [pii].

Causin, P., Gerbeau, J.F. and Nobile, F., 2005. "Added-mass effect in the design of partitioned algorithms for fluid-structure problems". *Computer Methods in Applied Mechanics and Engineering*, Vol. 194, No. 42-44, pp. 4506–4527. ISSN 00457825. doi:10.1016/j.cma.2004.12.005.

Cebral, J.R., Castro, M.A., Burgess, J.E., Putman, C.M., Pergolizzi, R.S. and Sheridan, M.J., 2005. "Characterization of Cerebral Aneurysms for Assessing Risk of Rupture by Using Patient-specific Computational Hemodynamics Models". *American Journ. Of Neuroradiology*, Vol. 26, pp. 2550–2559.

Cebral, J.R. and Cerrolaza, M., 2003. "Computational Analysis of Blood Flow Dynamics in Cerebral Aneurysms from CTA and 3D Rotational Angiography Image Data". In *International Congress on Computational Bioengineering*.

Degroote, J., Bathe, K.J. and Vierendeels, J., 2009. "Performance of a new partitioned procedure versus a monolithic procedure in fluid-structure interaction". *Computers and Structures*, Vol. 87, No. 11-12, pp. 793–801. ISSN 00457949.

- doi:10.1016/j.compstruc.2008.11.013. URL http://dx.doi.org/10.1016/j.compstruc.2008.11.013.
- Degroote, J., Bruggeman, P., Haelterman, R. and Vierendeels, J., 2008. "Stability of a coupling technique for partitioned solvers in FSI applications". *Computers and Structures*, Vol. 86, No. 23-24, pp. 2224–2234. ISSN 00457949. doi:10.1016/j.compstruc.2008.05.005. URL http://dx.doi.org/10.1016/j.compstruc.2008.05.005.
- Degroote, J., Haelterman, R., Annerel, S., Bruggeman, P. and Vierendeels, J., 2010. "Performance of partitioned procedures in fluid-structure interaction". *Computers and Structures*, Vol. 88, No. 7-8, pp. 446–457. ISSN 00457949. doi:10.1016/j.compstruc.2009.12.006. URL http://dx.doi.org/10.1016/j.compstruc.2009.12.006.
- Demirdžić, I. and Perić, M., 1988. "Space conservation law in finite volume calculations of fluid flow". *International Journal for Numerical Methods in Fluids*, Vol. 8, No. December 1987, pp. 1037–1050. ISSN 0271-2091. doi: 10.1002/fld.1650080906.
- Donea, J., Huerta, A., Ponthot, J. and Rodr, A., 1999. "Arbitrary Lagrangian Eulerian Methods". In *Encyclopedia of Computational Mechanics*, John Wiley & Sons, chapter 14, pp. 1–25. ISBN 0470846992. doi:10.1002/0470091355.ecm009.
- Evju, Ø., Valen-Sendstad, K. and Mardal, K.A., 2013. "A study of wall shear stress in 12 aneurysms with respect to different viscosity models and flow conditions". *Journal of Biomechanics*, Vol. 46, No. 16. ISSN 00219290. doi:10.1016/j.jbiomech.2013.09.004.
- Ford, M.D., Alperin, N., Lee, S.H., Holdsworth, D.W. and Steinman, D.A., 2005. "Characterization of normal cerebrovascular volumetric flow rate dynamics by PC-MRI". *The International Society for Magnetic Resonance in Medicine 13th Annual Meeting*, Vol. 13, p. 1741.
- Förster, C., Wall, W. and Ramm, E., 2006a. "The artificial added mass effect in sequential staggered fluid-structure interaction algorithms". *ECCOMAS CFD 2006: Proceedings of the European Conference on Computational Fluid Dynamics*, No. April, pp. 1–20.
- Förster, C., Wall, W.A. and Ramm, E., 2006b. "On the geometric conservation law in transient flow calculations on deforming domains". *International Journal for Numerical Methods in Fluids*, Vol. 50, No. 12, pp. 1369–1379. ISSN 02712091. doi:10.1002/fld.1093.
- Fukazawa, K., Ishida, F., Umeda, Y., Miura, Y., Shimosaka, S., Matsushima, S., Taki, W. and Suzuki, H., 2015. "Using computational fluid dynamics analysis to characterize local hemodynamic features of middle cerebral artery aneurysm rupture points". *World Neurosurgery*, Vol. 83, No. 1, pp. 80–86. ISSN 18788769. doi:10.1016/j.wneu.2013.02.012. URL http://dx.doi.org/10.1016/j.wneu.2013.02.012.
- Gijn, J.V. and Rinkel, G.J.E., 2001. "Subarachnoid haemorrhage: diagnosis, causes and management." *Brain: a journal of neurology*, Vol. 124, No. Pt 2, pp. 249–78. ISSN 0006-8950. doi:10.1093/brain/124.2.249. URL http://www.ncbi.nlm.nih.gov/pubmed/11157554.
- Hop, J.W., Rinkel, G.J., Algra, A. and van Gijn, J., 1997. "Case-Fatality Rates and Functional Outcome After Subarachnoid Hemorrhage: A Systematic Review". *Stroke*, Vol. 28, No. 3, pp. 660–664. ISSN 0039-2499. doi: 10.1161/01.STR.28.3.660. URL http://stroke.ahajournals.org/cgi/content/long/28/3/660.
- Isaksen, J.G., Bazilevs, Y., Kvamsdal, T., Zhang, Y., Kaspersen, J.H., Waterloo, K., Romner, B. and Ingebrigtsen, T., 2008. "Determination of wall tension in cerebral artery aneurysms by numerical simulation". *Stroke*, Vol. 39, No. 12, pp. 3172–3178. ISSN 00392499. doi:10.1161/STROKEAHA.107.503698.
- Jasak, H. and Tuković, Ž., 2006. "Automatic mesh motion for the unstructured Finite Volume Method". *Transactions of Famena*, Vol. 30, No. 2, pp. 1–20. ISSN 13331124. doi:10.1126/science.1247727.
- Karmonik, C., Diaz, O., Klucznik, R., Grossman, R.G., Zhang, Y.J., Britz, G., Lv, N. and Huang, Q., 2014. "Quantitative comparison of hemodynamic parameters from steady and transient CFD simulations in cerebral aneurysms with focus on the aneurysm ostium." *Journal of neurointerventional surgery*, pp. 1–6. ISSN 1759-8486. doi:10.1136/neurintsurg-2014-011182. URL http://jnis.bmj.com/content/early/2014/04/10/neurintsurg-2014-011182.long.
- Lee, C.J., Zhang, Y., Takao, H., Murayama, Y. and Qian, Y., 2013. "A fluid–structure interaction study using patient-specific ruptured and unruptured aneurysm: The effect of aneurysm morphology, hypertension and elasticity". *Journal of Biomechanics*, Vol. 46, pp. 2402–2410. doi:10.1002/cnm.1396.
- Lu, G., Huang, L., Zhang, X.L., Wang, S.Z., Hong, Y., Hu, Z. and Geng, D.Y., 2011. "Influence of hemodynamic factors on rupture of intracranial aneurysms: Patient-specific 3D mirror aneurysms model computational fluid dynamics simulation". *American Journal of Neuroradiology*, Vol. 32, No. 7, pp. 1255–1261. ISSN 01956108. doi:10.3174/ajnr.A2461.
- Meng, H., Tutino, V.M., Xiang, J. and Siddiqui, A., 2014. "High WSS or Low WSS? Complex interactions of hemodynamics with intracranial aneurysm initiation, growth, and rupture: Toward a unifying hypothesis". *American Journal of Neuroradiology*, Vol. 35, No. 7, pp. 1254–1262. ISSN 1936959X. doi:10.3174/ajnr.A3558.
- Moukalled, F., Mangani, L. and Darwish, M., 2016. *The Finite Volume Method in Computational Fluid Dynamics*, Vol. 113. Springer. ISBN 978-3-319-16873-9. doi:10.1007/978-3-319-16874-6.
- Oberkampf, W.L. and Trucano, T.G., 2002. "Verification and validation in computational fluid dynamics". *Progress in Aerospace Sciences*, Vol. 38, No. 3, pp. 209–272. ISSN 03760421. doi:10.1016/S0376-0421(02)00005-2.
- OpenFOAM-Extend, 2017. "foam-extend Website". https://sourceforge.net/projects/foam-extend/. [Accessed 19-June-2017].

- Patankar, S., 1980. *Numerical heat transfer and fluid flow*. McGraw-Hill Publishing. ISBN 978-0891165224 0. doi: 10.1016/j.watres.2009.11.010.
- Penn, D.L., Komotar, R.J. and Sander Connolly, E., 2011. "Hemodynamic mechanisms underlying cerebral aneurysm pathogenesis". *Journal of Clinical Neuroscience*, Vol. 18, No. 11, pp. 1435–1438. ISSN 09675868. doi: 10.1016/j.jocn.2011.05.001. URL http://dx.doi.org/10.1016/j.jocn.2011.05.001.
- Qureshi, A.I., Janardhan, V., Hanel, R.A. and Lanzino, G., 2007. "Comparison of endovascular and surgical treatments for intracranial aneurysms: an evidence-based review". *Lancet Neurology*, Vol. 6, No. 9, pp. 816–825. ISSN 14744422. doi:10.1016/S1474-4422(07)70217-X.
- Shojima, M., Oshima, M., Takagi, K., Torii, R., Hayakawa, M., Katada, K., Morita, A. and Kirino, T., 2004. "Magnitude and Role of Wall Shear Stress on Cerebral Aneurysm: Computational Fluid Dynamic Study of 20 Middle Cerebral Artery Aneurysms". *Stroke*, Vol. 35, No. 11, pp. 2500–2505. ISSN 0039-2499. doi:10.1161/01.STR.0000144648.89172.0f.
- Steinman, D.A., Milner, J.S., Norley, C.J., Lownie, S.P. and Holdsworth, D.W., 2003. "Image-based computational simulation of flow dynamics in a giant intracranial aneurysm." *AJNR. American journal of neuroradiology*, Vol. 24, No. 4, pp. 559–66. ISSN 0195-6108. URL http://www.ajnr.org/content/24/4/559.abstract.
- The International Study of Unruptured Intracranial Aneurysms Investigators, 2003. "Unruptured intracranial aneurysms: natural history, clinical outcome, and risks of surgical and endovascular treatment". *Lancet*, Vol. 362, pp. 103–110. ISSN 1474-547X. doi:10.1016/S0140-6736(03)13860-3.
- Torii, R., Oshima, M., Kobayashi, T., Takagi, K. and Tezduyar, T.E., 2006. "Fluid-structure interaction modeling of aneurysmal conditions with high and normal blood pressures". *Computational Mechanics*, Vol. 38, No. 4-5, pp. 482–490. ISSN 01787675. doi:10.1007/s00466-006-0065-6.
- Torii, R., Oshima, M., Kobayashi, T., Takagi, K. and Tezduyar, T.E., 2007. "Influence of wall elasticity in patient-specific hemodynamic simulations". *Computers and Fluids*, Vol. 36, No. 1, pp. 160–168. ISSN 00457930. doi: 10.1016/j.compfluid.2005.07.014.
- Torii, R., Oshima, M., Kobayashi, T., Takagi, K. and Tezduyar, T.E., 2008. "Fluid-structure interaction modeling of a patient-specific cerebral aneurysm: Influence of structural modeling". *Computational Mechanics*, Vol. 43, No. 1, pp. 151–159. ISSN 01787675. doi:10.1007/s00466-008-0325-8.
- Torii, R., Oshima, M., Kobayashi, T., Takagi, K. and Tezduyar, T.E., 2009. "Fluid-structure interaction modeling of blood flow and cerebral aneurysm: Significance of artery and aneurysm shapes". *Computer Methods in Applied Mechanics and Engineering*, Vol. 198, No. 45-46, pp. 3613–3621. ISSN 00457825. doi:10.1016/j.cma.2008.08.020. URL http://dx.doi.org/10.1016/j.cma.2008.08.020.
- Tricerri, P., Dedè, L., Deparis, S., Quarteroni, A., Robertson, A.M., Sequeira, A., Tricerri, P., Dedè, L., Deparis, S., Quarteroni, A., Sequeira, A. and Robertson, A.M., 2015. "Fluid-structure interaction simulations of cerebral arteries modeled by isotropic and anisotropic constitutive laws". *Computational Mechanics*, Vol. 55, No. 3, pp. 479–498. ISSN 01787675. doi:10.1007/s00466-014-1117-y.
- van Gijn, J., Kerr, R.S. and Rinkel, G.J.E., 2007. "Subarachnoid haemorrhage." *Lancet*, Vol. 369, No. 9558, pp. 306–318. ISSN 1474-547X. doi:10.1016/S0140-6736(07)60153-6.
- Versteeg, H.K. and Malalasekera, W., 2007. *An Introduction to Computational Fluid Dynamics*, Vol. 1. Pearson Prentice Hall. ISBN 9780131274983.
- Wong, G.K.C. and Poon, W.S., 2011. "Current status of computational fluid dynamics for cerebral aneurysms: The clinician's perspective". *Journal of Clinical Neuroscience*, Vol. 18, No. 10, pp. 1285–1288. ISSN 09675868. doi: 10.1016/j.jocn.2011.02.014.
- Zacharia, B.E., Hickman, Z.L., Grobelny, B.T., DeRosa, P., Kotchetkov, I., Ducruet, A.F. and Connolly, E.S., 2010. "Epidemiology of Aneurysmal Subarachnoid Hemorrhage". *Neurosurgery Clinics of North America*, Vol. 21, No. 2, pp. 221–233. ISSN 10423680. doi:10.1016/j.nec.2009.10.002.
- Zarrinkoob, L., Ambarki, K., Wåhlin, A., Birgander, R., Eklund, A. and Malm, J., 2015. "Blood flow distribution in cerebral arteries." *Journal of cerebral blood flow and metabolism*, Vol. 35, pp. 648–654. ISSN 1559-7016. doi:10.1038/jcbfm.2014.241. URL http://www.ncbi.nlm.nih.gov/pubmed/25564234.

# 7. RESPONSIBILITY NOTICE

The authors are the only responsible for the printed material included in this paper.